Geophysical Journal International

Geophys. J. Int. (2025) **242,** 1–12
Advance Access publication 2025 June 24
Research Paper

https://doi.org/10.1093/gji/ggaf238

The SOLA method for the inversion of induced polarization data

Williams Lima[1] and Christophe Zaroli[2]

[1]*Federal University of Rio Grande do Norte, Physics, Campus Universitário Lagoa Nova, Natal - RN,* 59078-970*, Brazil. E-mail: dwilliams.lima@gmail.com*
[2]*Institut Terre et Environnement de Strasbourg, Université de Strasbourg, EOST, CNRS, UMR* 7063*,* 5 *rue Descartes, Strasbourg F-*67084*, France*

Accepted 2025 June 20. Received 2025 May 15; in original form 2025 January 16

SUMMARY

Inversion of a given geophysical data set cannot be complete without assessing the resolution and uncertainties associated with the model obtained. However, model appraisal may still be a challenging task from both a theoretical and a computational point of view. To tackle the problems of model estimation and appraisal, we introduce the subtractive optimally localized averages (SOLA) method to the geophysical electromagnetic community, through the example of linear inversion of induced polarization (IP) data. SOLA is a variant of the Backus-Gilbert method: it is computationally more efficient but also allows one to specify directly the target local averages of the Earth's properties to be estimated, including their uncertainties. SOLA offers great flexibility in the construction of averaging kernels, via the design of target kernels, and direct control over the propagation of data errors into the local-average estimates. With SOLA we obtain a collection of (i) local averages of the 'true' Earth model, accompanied with their (ii) averaging kernels and (iii) uncertainties. We investigated the performance of SOLA for the 2-D tomographic inversion of a field IP data set. The obtained chargeability model compares well with previous studies, and, most importantly, its resolution (the spatial extent of the averaging kernels) and uncertainties can be interrogated. We conclude that SOLA is a promising approach for geophysical-electromagnetic linear(ized) tomographies. In the case of IP inversion, to construct chargeability models and evaluate their robustness.

Key words: Electrical resistivity tomography (ERT); Induced polarization; Inverse theory.

1 INTRODUCTION

The resolving power of geophysical data to estimate the parameters of Earth models is notoriously limited (e.g. Jackson 1972). A complete treatment of the inverse problem should then include model estimation *and* model assessment, giving equal importance to both the reconstruction of a geologically meaningful Earth model and the assessment of its uncertainties (in a general sense). For linear or linearizable inverse problems, both model reconstruction and model assessment are epitomized by the generalized inverse and the corresponding model resolution and covariance matrices derived from it (e.g. Aster *et al.* 2018). Together, these mathematical objects allow for a complete treatment of the linear inverse problem. The subtractive optimally localized averages (SOLA) method (Pijpers & Thompson 1992) is a variant of the Backus–Gilbert (BG) method (Backus & Gilbert 1967, 1968, 1970). Although both SOLA and BG aim at directly estimating the generalized inverse coefficients, SOLA is computationally more efficient and allows one to specify directly the 'target' local averages of the Earth's properties to be estimated, including their uncertainties. SOLA was first introduced in astronomy for solving 1-D helioseismic inversions (e.g. Pijpers & Thompson 1994; Pijpers 1997). Recently, it has been successfully adapted to solve large-scale 2-D and 3-D (both discrete and continuous) seismic tomography problems (Zaroli 2016, 2019; Zaroli *et al.* 2017). In this work, we investigate the applicability of SOLA for 2-D linear tomographic inversion of induced polarization (IP) data. To the best of our knowledge, this is the first time that SOLA has been used for geophysical-electromagnetic tomography. This paper begins with a simplified review of the Backus–Gilbert method. Next, we introduce SOLA followed by a short treatment of the induced polarization theory relevant to this work. We illustrate these theoretical aspects with a synthetic IP data based example, and then an application to a real field IP data from a mining region in Australia. We conclude with a discussion on the relevance of SOLA for inverting IP data —and for quantifying the robustness of chargeability model features via quantitative resolution–uncertainty analysis.

2 THE BACKUS–GILBERT METHOD

The Backus–Gilbert (BG) method was introduced in a series of seminal papers half a century ago (Backus & Gilbert 1967, 1968, 1970), with focus on linear geophysical inverse problems. Backus and Gilbert proposed a different perspective for approaching the problem of geophysical inversion in comparison to the more widely known, in one form or another, regularization method of Tikhonov

(Tikhonov & Arsenin 1977). Instead of aiming at solving the estimation problem, where an approximation for the true (unknown) solution is sought, the BG method intrinsically develops tools for the quantitative analysis of the resolution power of the available data. Therefore, it brings the estimation of the information content of the data to the forefront of the problem of geophysical data inversion.

The BG approach philosophically contrasts with the 'find a solution that fits the data' approach of conventional inversion methods. Since its inception, the theoretical aspects of the BG method have always attracted the interest of the scientific community (e.g. in pure and applied mathematics and geophysics); with the appearance of many interesting reviews (e.g. Haario & Somersalo 1987; Kirsch *et al.* 1988; Snieder 1991; Leitão 1998; Pujol 2013; Aster *et al.* 2018). On the other hand, the method has never been popular in practical applications such as in geophysics, especially when compared with Tikhonov regularization methods. The main reason for that was the computational cost of the method, a concern well justified in the past decades but that certainly needs to be reviewed today, after decades of evolution in computing power. As we shall see, a variant of BG, the so-called SOLA method, has proven to be computationally more efficient than BG, while still allowing one to benefit fully from the advantages of BG. The BG theory is constructed around three main concepts: (i) linear model averages, and their corresponding (ii) averaging kernels and (iii) uncertainties.

Let's assume that we have specified, for our geophysical purposes, an abstract representation of the Earth model as a function $m \in L^2(\Omega)$, $\Omega \subset \mathbb{R}^2$, where $L^2(\Omega)$ is the space of square integrable functions defined in the domain Ω; here $\Omega \subset \mathbb{R}^2$ refers to a 2-D space (2-D subsurface), as in the example of SOLA IP tomography conducted in this study. The relation between m and the physical quantities representing the N geophysical measurements is specified by a set of N functions (BG and SOLA only consider linear or linearizable ones), the so-called gross Earth functionals: $g = \{g_i\} \in \mathbb{R}^N$. Each $g_i \in L^2(\Omega)$ is given by:

$$g_i[m] = \int_\Omega G_i(\mathbf{r}) m(\mathbf{r}) \mathrm{d}^2\mathbf{r}\,, \tag{1}$$

where each function $G_i \in L^2(\Omega)$ is called a data kernel ($i = 1 \cdots N$). In practice, we only have access to a finite set of N noisy measurements $d = \{d_i\} \in \mathbb{R}^N$. Each so-called gross Earth datum can then be written as:

$$d_i = g_i[m] + n_i\,, \tag{2}$$

where n_i is the ith noise component. In this study, we shall assume zero-mean, independent, Gaussian noise, that is, a diagonal data covariance matrix with entries $\sigma_{d_i}^2$. In the BG theory, we aim at estimating a (weighted) local average, $\hat{m}_k$, of the 'true' Earth model, $m(\mathbf{r})$, around a specified position, $\mathbf{r}_k$, in the domain Ω. The local-average estimate $\hat{m}_k$ is sought as a linear combination of the data:

$$\hat{m}_k = \sum_{i=1}^{N} x_i^{(k)} d_i\,, \tag{3}$$

where the N real-valued $x_i^{(k)}$ represent generalized inverse coefficients—these coefficients are the unknowns which are directly solved for in BG (and SOLA). The average estimate $\hat{m}_k$ can therefore be expressed as:

$$\hat{m}_k = \underbrace{\int_\Omega A^{(k)}(\mathbf{r}) m(\mathbf{r}) \mathrm{d}^2\mathbf{r}}_{\text{averaging process}} + \underbrace{\sum_{i=1}^{N} x_i^{(k)} n_i}_{\text{noise propagation}}\,, \tag{4}$$

where the averaging kernel function $A^{(k)}(\mathbf{r})$ is given by:

$$A^{(k)}(\mathbf{r}) = \sum_{i=1}^{N} x_i^{(k)} G_i(\mathbf{r})\,. \tag{5}$$

The averaging kernel $A^{(k)}(\mathbf{r})$ is also referred to as the resolving kernel (e.g. Zaroli 2016; Zaroli *et al.* 2017); its spatial support is a measure of the achieved resolution around the enquiry point $\mathbf{r}_k$. As we shall see, the ideal situation for Backus–Gilbert (SOLA) theory would be for $A^{(k)}$ to resemble a Dirac-delta function (or a pre-defined target function), respectively. The noise propagation in (4) can be statistically described by a zero-mean normal distribution with variance:

$$\sigma_{\hat{m}_k}^2 = \sum_{i=1}^{N} \left(x_i^{(k)} \sigma_{d_i} \right)^2\,. \tag{6}$$

The standard deviation $\sigma_{\hat{m}_k}$ represents the uncertainty attached to the average estimate $\hat{m}_k$. In the BG method, the functions $A^{(k)}(\mathbf{r})$ are constrained to be unimodular, that is:

$$\int_\Omega A^{(k)}(\mathbf{r}) \mathrm{d}^2\mathbf{r} = 1\,. \tag{7}$$

The explicit imposition of the unimodular constraint (7) is to force the average estimate $\hat{m}_k$ to be unbiased, a fundamental property of the BG (and SOLA) averaging kernels—not always honoured with Tikhonov methods (e.g. Nolet 2008; Zaroli *et al.* 2017). The estimate $\hat{m}_k$, averaging kernel $A^{(k)}$, and uncertainty $\sigma_{\hat{m}_k}$ are all dependent on the set of N generalized-inverse coefficients $\mathbf{x}^{(k)} = \{x_i^{(k)}\}_{i=1}^N$. Given P, the number of enquiry points $\mathbf{r}_k$ in the domain Ω, to build a model with BG (and SOLA) thus consists in calculating a collection of P estimates $\{\hat{m}_k\}_{k=1}^P$. Though these estimates are independently obtained—and thus can be computed in an embarrassingly parallel fashion—it is possible to build a model (i.e. a collection of estimates) which can fit the data, at least with the SOLA approach (Zaroli 2016, 2021; Zaroli *et al.* 2017). In summary, we perform an inversion at each of the P enquiry points $\mathbf{r}_k$ for the generalized-inverse coefficients $\mathbf{x}^{(k)} \in \mathbb{R}^N$, from which we obtain a collection of P local-average estimates, averaging kernels and uncertainties. Note that each of the P independent inversions has N unknowns.

The rationale in the BG method is to find a set $\mathbf{x}^{(k)}$ such that the averaging kernel $A^{(k)}$ approaches a Dirac delta function $\delta(\mathbf{r} - \mathbf{r}_k)$, centred on the position $\mathbf{r}_k$. With this objective in mind, Backus and Gilbert seek $\mathbf{x}^{(k)}$ such that it leads to minimizing both the spatial spread of $A^{(k)}$ and the uncertainty $\sigma_{\hat{m}_k}$, while honouring the unimodular constraint. This can be cast in the following optimization problem:

$$\begin{cases} \underset{\mathbf{x}^{(k)} \in \mathbb{R}^N}{\arg\ \min:}\ S^{(k)} + \eta^2 \sigma_{\hat{m}_k}^2 \\ \text{s.t.} \qquad \int_\Omega A^{(k)}(\mathbf{r})\, \mathrm{d}^2\mathbf{r} = 1\,, \end{cases} \tag{8}$$

The so-called *spread functional* $S^{(k)}$ is defined as:

$$S^{(k)} = \int_\Omega \left[A^{(k)}(\mathbf{r}) \right]^2 J^{(k)}(\mathbf{r}) \mathrm{d}^2\mathbf{r}\,. \tag{9}$$

It is aimed at representing the spatial extent of $A^{(k)}$. Thus, the function $J^{(k)}$ in (9) is defined as follows:

$$J^{(k)}(\mathbf{r}) \propto |\mathbf{r} - \mathbf{r}_k|^p\,. \tag{10}$$

As a remark, if the shape of $A^{(k)}$ were close to a 2-D disc, $S^{(k)}$ would represent the disc's diameter. In (10), p is an integer to be chosen such that $S^{(k)}$ represents a length; for our 2-D IP tomography application: $p = 3$. The hyperparameter $\eta \in \mathbb{R}_+$ in (8) reflects the unavoidable trade-off between resolution and uncertainty. It

balances the desire to have a localized kernel $A^{(k)}$ (here close to a Dirac delta), against the pernicious effect of the propagation of data errors into the estimate $\hat{m}_k$. The trade-off parameter η can be kept constant, with a potential reduction in the computational cost, or can be allowed to vary for each query point $\mathbf{r}_k$; in this study we shall consider it to be spatially variant and offer one possible strategy to automatize the choice of its values. Having stated the basic facts about the BG method, we now move on to a short description of its SOLA variant—which we aim at using for the inversion of field IP data, for the very first time.

3 THE SOLA METHOD

One primary motivation for preferring to use SOLA, rather than BG, is the fact that the computational cost of solving (8) can be greatly reduced by the introduction of *target kernels* (Pijpers & Thompson 1992; Zaroli 2016, 2019). Instead of trying to approximate the averaging kernel to a Dirac delta, SOLA specifies an *a priori* target kernel function $T^{(k)}(\mathbf{r})$ for each averaging kernel function $A^{(k)}(\mathbf{r})$. Note that this is fundamentally different from adding *a priori* information on the model itself, as in Tikhonov regularization methods (Tarantola 2006). In practice, this is accomplished by modifying the spread functional $S^{(k)}$ in (8). This leads to the SOLA optimization problem:

$$\begin{cases} \underset{\mathbf{x}^{(k)}\in\mathbb{R}^N}{\arg\ \min}\colon \hat{S}^{(k)} + \eta^2\,\sigma^2_{\hat{m}_k} \\ \text{s.t.} \qquad \int_\Omega A^{(k)}(\mathbf{r})\,\mathrm{d}^2\mathbf{r} = 1\,, \end{cases} \tag{11}$$

where the *resolution-misfit* functional $\hat{S}^{(k)}$ is defined as:

$$\hat{S}^{(k)} = \int_\Omega \left[A^{(k)}(\mathbf{r}) - T^{(k)}(\mathbf{r})\right]^2 \mathrm{d}^2\mathbf{r}\,, \tag{12}$$

from where the term 'subtractive', of the SOLA acronym, becomes apparent. In this work, we shall use 2-D disc-shaped target kernels:

$$T^{(k)}(\mathbf{r}\in\Omega) = \begin{cases} \frac{1}{\pi\times(\ell_k)^2} & \text{if} \quad |\mathbf{r}-\mathbf{r}_k| \le \ell_k \\ 0 & \text{elsewhere}\,, \end{cases} \tag{13}$$

where ℓ_k denotes the disc's radius, and thus represents the *a priori* (isotropic) resolving length at the location $\mathbf{r}_k$. This choice, that is, (13), corresponds to the following normalization of $T^{(k)}$:

$$\int_\Omega T^{(k)}(\mathbf{r})\mathrm{d}^2\mathbf{r} = 1\,. \tag{14}$$

Other choices of target kernel (e.g. 2-D Gaussian) and normalization could be investigated (e.g. Freissler *et al.* 2024; Mag *et al.* 2025). Most importantly, replacing the spread functional $S^{(k)}$ by the resolution-misfit functional $\hat{S}^{(k)}$ leads to multiple benefits: (i) it adds a degree of freedom to the method allowing the user to choose the target kernels according to the characteristics of the problem at hand, and (ii) it decreases the computational cost of the optimization problem to be solved for $\mathbf{x}^{(k)}$.

In this study, for improving the computational efficiency of SOLA, we shall use its *discrete* version for our application to field IP data inversion. That is, the model space (Ω) will have to be discretized, similarly to conventional (data-fit based) tomographic methods, which generally take place in a discrete fashion. For example, in the 2-D IP tomography applications presented in Sections 5 and 6 the model space is discretized with M 'cells'. This implies that we have to consider the projection of the N continuous data kernels G_i on the tomographic grid, which results in the classic sensitivity matrix $\mathbf{G} = (G_{ij})$ of size $N \times M$. We refer the reader to Zaroli (2016) for explanations about the technical details and numerical advices involved in setting up and solving the 'discrete' form of the SOLA problem. However, in the following we provide some details to explain the main computational advantage of SOLA with respect to BG. First, note that both the BG and SOLA problems numerically consist in solving for the generalized-inverse coefficients $\mathbf{x}^{(k)}$ a linear system grossly of the form:

$$\mathbf{matrix}^{BG/SOLA}\,\mathbf{x}^{(k)} \;=\; \mathbf{vector}^{BG/SOLA}\,. \tag{15}$$

The dominant computational task to set up (15) is the calculation of the matrix itself. Importantly, $\mathbf{matrix}^{BG}$ ($\mathbf{matrix}^{SOLA}$) needs (*not*) to be recalculated for each query point, $\mathbf{r}_k$, respectively (Pijpers & Thompson 1992; Zaroli 2016, 2019). To have a better understanding of this last point, note that the BG optimization problem (8) results in the following constrained minimization problem to be solved for the generalized-inverse coefficients $\mathbf{x}^{(k)}$ (Zaroli 2016):

$$\left(\hat{\mathbf{G}}^{(k)}(\hat{\mathbf{G}}^{(k)})^T + \eta^2\mathbf{I}_N\right)\mathbf{x}^{(k)} = \mathbf{0}_N\,, \quad \text{subject to} \quad \mathbf{c}^T\mathbf{x}^{(k)} = 1\,, \tag{16}$$

where the dependence in the location $\mathbf{r}_k$ of the considered enquiry point is contained in the matrix:

$$\hat{\mathbf{G}}^{(k)} = \left(\frac{|\mathbf{r}^{(j)} - \mathbf{r}_k|^2}{\sqrt{\mathbb{V}_j}}\,G_{ij}\right)\,, \quad 1 \le i \le N\,, \quad 1 \le j \le M\,. \tag{17}$$

where $\mathbf{r}^{(j)}$ and $\mathbf{r}_k$ represent the spatial locations of the central points of the jth and kth cells of our 2-D tomographic grid, $\mathbb{V}_j$ represents the area of the jth cell and the vector $\mathbf{c} = (c_i)_{1\le i\le N}$ has elements: $c_i = \sum_{j=1}^{M} G_{ij}$. The condition $\mathbf{c}^T\mathbf{x}^{(k)} = 1$ in the eq. (16) reflects the fact that we want to achieve the unimodularity of the averaging kernel, that is, eq. (7). On the other hand, the SOLA optimization problem (11) leads to solving for $\mathbf{x}^{(k)}$ this different constrained minimization problem (Zaroli 2016):

$$\left(\hat{\mathbf{G}}\hat{\mathbf{G}}^T + \eta^2\mathbf{I}_N\right)\mathbf{x}^{(k)} = \hat{\mathbf{G}}\mathbf{t}^{(k)}\,, \quad \text{subject to} \quad \mathbf{c}^T\mathbf{x}^{(k)} = 1\,, \tag{18}$$

where the dependence in the enquiry point's location $\mathbf{r}_k$ is *not* contained in the new matrix:

$$\hat{\mathbf{G}} = \left(\frac{1}{\sqrt{\mathbb{V}_j}}\,G_{ij}\right)\,, \quad 1 \le i \le N\,, \quad 1 \le j \le M\,. \tag{19}$$

This represents a crucial computational advantage with regard to setting up the BG matrix (17). That is, we do *not* have to recompute the SOLA matrix for each new enquiry point. The vector $\mathbf{t}^{(k)} = (T^{(k)}_j\sqrt{\mathbb{V}_j})_{1\le j\le M}$ in eq. (18) mainly contains the M components $T^{(k)}_j$ resulting from the projection of the target kernel $T^{(k)}$ on the tomographic grid. The task of computing the target kernel, that is, $\mathbf{t}^{(k)}$, is not at all computationally demanding. As previously mentioned, we refer the reader to Zaroli (2016)'s Appendix A which contains all numerical explanations required to solve efficiently the SOLA system (18), using the LSQR iterative row action method (Paige & Saunders 1982)—including mathematical notations consistent with those employed in this study.

Finally, we emphasize that all what is needed for to get started with *discrete SOLA tomography*, in addition to the data and their uncertainties, is: (i) the same sensitivity matrix (denoted $\mathbf{G}$) as for conventional tomography, and (ii) an estimation of the *a priori* local resolution, to infer the size of target kernels, which may be based on simple proxies reflecting the data coverage. It should then be 'straightforward' to move from conventional- to SOLA-based discrete IP tomography.

4 INDUCED POLARIZATION MODELLING

The phenomenon of induced polarization (IP) is today an extensively studied subject in geophysics, with very important applications in sectors such as mining, environment, oil & gas, etc. Due to this importance, many works have been dedicated to the analysis of its theoretical, computational and application aspects for at least 70 yr now (e.g. Bleil 1953; Hallof 1957; Vacquier *et al.* 1957; Marshall & Madden 1959; Seigel 1959; Sumner 1976; Angoran & Madden 1977; Rijo 1984; Oldenburg & Li 1994; Li & Oldenburg 2000; Gurin *et al.* 2015; Ahmed *et al.* 2020; Revil *et al.* 2024). In this work, we follow the mathematical formulation described in Oldenburg & Li (1994) and Li & Oldenburg (2000). For numerical simulations, we used the open source Python package SimPEG (Cockett *et al.* 2015) which has a comprehensive set of flexible and efficient codes for modelling/inversion of 2-D/2.5-D/3-D DC (Direct Current) Resistivity and IP data. Although a very interesting topic in itself, it is not our objective to do a review of the IP geophysical method here, so we limit ourselves to the descriptions of fundamental relations used in this work; the reader interested in a complete treatment of the theory, application and computational aspects of IP will surely find more than enough information in the references cited above and the references therein. We describe here the aspects of forward modelling in a 3-D Earth and will revert to a 2-D Earth later when describing the numerical experiments.

Let our Earth model be specified by the two physical properties, electric conductivity $\sigma(x, y, z)$ and chargeability $\eta(x, y, z)$. In the linearized approach used in this work, the IP forward/inverse problem is formulated as a two-stage process (Li & Oldenburg 2000). First, a DC resistivity inversion is carried out to recover the background conductivity of the medium. Then the sensitivity matrix for the DC problem is computed, using this background conductivity. This sensitivity matrix will then be used to specify the forward IP problem as described below.

Following Oldenburg & Li (1994), the PDE governing the DC electric potential ϕ_σ is given by

$$\begin{cases} \nabla \cdot (\sigma \nabla \phi_\sigma) = -I\delta(\mathbf{r} - \mathbf{r}_s) & \text{in} \quad \Omega \\ \partial_n \phi_\sigma = 0 & \text{in} \quad \partial\Omega\,, \end{cases} \tag{20}$$

where I is the amplitude of the electrical current injected in the subsurface at position $\mathbf{r}_s$. This PDE implicitly defines the forward operator $F_{dc}[\sigma]$ for computing the DC potentials ϕ_σ such that:

$$\phi_\sigma = F_{dc}[\sigma]. \tag{21}$$

In turn, for computing the IP potentials, we assume that the effect of the chargeability is to change the effective conductivity of the medium (Li & Oldenburg 2000). The IP potential ϕ_η is obtained using the same DC forward operator F_{dc}, this time replacing σ by $\sigma(1 - \eta)$, that is:

$$\phi_\eta = F_{dc}[\sigma(1 - \eta)]\,. \tag{22}$$

The actual IP data used for inversion is the apparent chargeability, defined as follows:

$$\eta_a = \frac{\phi_s}{\phi_\eta} = \frac{\phi_\eta - \phi_\sigma}{\phi_\eta}\,, \tag{23}$$

where $\phi_s = \phi_\eta - \phi_\sigma$ is the measured IP secondary potential. Now, under the assumption of moderate magnitude of the chargeability η, ϕ_η is linearized with respect to a background conductivity σ (Oldenburg & Li 1994), thus leading to:

$$\eta_{a_i} = \sum_j -\frac{\partial \ln \phi_{\eta_i}}{\partial \ln \sigma_j}\eta_j = \sum_j G_{ij}\eta_j\,, \tag{24}$$

where $G_{ij} = -\frac{\partial \ln \phi_{\eta_i}}{\partial \ln \sigma_j}$ is the sensitivity matrix ($i = 1 \cdots N$, $j = 1 \cdots M$) used subsequently for the IP inversion. Finally, the IP forward problem can be put in the form of a linear system:

$$\mathbf{d} = \mathbf{G}\mathbf{m}\,, \tag{25}$$

where the vector $\mathbf{d}$ (N data) corresponds to the measured apparent chargeability η_a, and the vector $\mathbf{m}$ (M model parameters) represents the intrinsic chargeability η.

In this work, we took advantage of SimPEG (Cockett *et al.* 2015) for computations related to the solution of DC resistivity, IP forward problems and the computation of IP sensitivity matrices. For the 2-D case, the computational domain was discretized using a regular grid with σ and η specified at the cell centres of this mesh. Forward codes use a 2.5-D formulation to deal with the three-dimensionality of the sources in a 2-D medium. We refer the interested reader to the SimPEG documentation and tutorials publicly available on the project's website (https://simpeg.xyz/).

5 SYNTHETIC DATA EXAMPLE

5.1 Geological model and data

We show in Fig. 1(a) a simple earth model to illustrate some key elements of the SOLA approach. This model is based on a fractal pattern known as the 'Sierpinski carpet', it is similar to the popular checkerboard pattern used in many studies related to geophysical inversion. The sizes of the perturbations in this model vary throughout the inversion domain, which makes it particularly interesting for resolution analyses like those proposed in this work. All blocks have the same chargeability values of 0.2 inserted in a background medium with electrical conductivity and chargeability equal to 10^{-2} S m^{-1} and 10^{-6}, respectively. We defined a dipole–dipole survey line distributed along the surface in the interval $[-20, 20]$ m with a spacing of 1 m between stations. The grid used to generate the data is based on a central region $\Omega = [-8, 0]\,\text{m} \times [-20, 20]\,\text{m}$, discretized as a regular grid; this region was extended using a quad-tree mesh in the horizontal directions and at the bottom of the model to avoid boundary artefacts (Fig. 2). Moreover, Fig. 3 presents a selection of rows from the sensitivity matrix $\mathbf{G}$, illustrating data-sensitivity kernels projected onto the modelling grid. Additionally, 5 per cent Gaussian noise was added to the computed data. Fig. 1(b) displays the IP data for the entire survey.

5.2 Gallery of SOLA averaging kernels

We show in Fig. 4 nine SOLA averaging kernels for a point located at coordinates $\mathbf{r}_k = (x, z) = (0, -1)$. We selected 2-D disc-shaped target kernels $T^{(k)}$ with varying radius ℓ_k, centred on the same enquiry point $\mathbf{r}_k$; the radius ℓ_k represents the *a priori* local resolving length. The columns are associated with different values for the trade-off parameter ($\eta = 1, 20, 30$); the rows show different target kernel sizes ($\ell_k = 0.1, 0.5, 1.5$ m). The purpose of this analysis is to decide on the optimum values for the target kernel size and the trade-off parameter for this particular point. In this example, the interpreter could choose a combination with the smallest kernel size which still has an acceptable error level (say 10 per cent relative to the estimated average), in this case the one in Fig. 4(e); this error

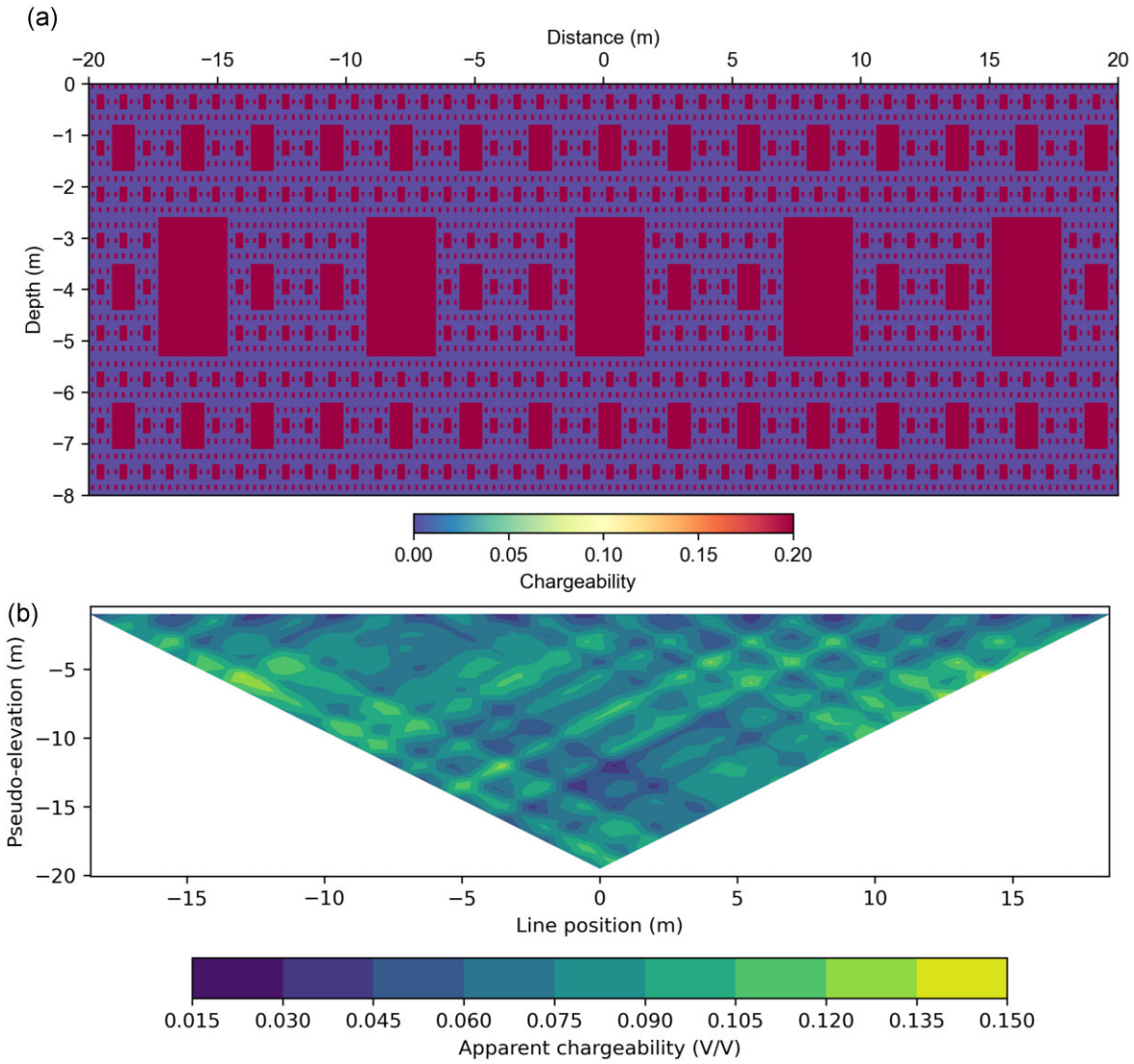

Figure 1. 'Toy' experiment: (a) Chargeability 'true' model (Sierpinski-carpet fractal pattern), and (b) IP data.

level, we must emphasize, is decided by the interpreter. Once we have an initial informed estimate for the trade-off parameters and the size of the target kernel, we can proceed with the analysis in the target domain, computing the SOLA estimates for all cells within the region Ω.

5.3 SOLA inversion results in the target area Ω

Based on the analysis of the previous section, we ran the SOLA algorithm in the target region Ω. This time, we used a different (coarser) grid for the inversion compared to the finer grid used to compute the data. The use of a coarser grid significantly reduces the total execution time while also aligning better with the actual resolution expected from the results obtained in the previous section. This ensures that the inversion process is computationally efficient without compromising the reliability of the results. The outcome of this inversion is presented in Fig. 5(b), where we also show the ground-truth model in Fig. 5(a) and the result obtained running SimPEG inversion code (Fig. 5c), for reference.

The values for the trade-off parameter and the target kernel size are generally spatially dependent, reflecting variations in the data sensitivity across the target region. For this test, we adopted the interpolation strategy described in Zaroli (2021), which is based on the computed sensitivity matrix. This approach allows for the effective interpolation of both the trade-off parameter and the target kernel sizes, ensuring coherent values throughout the domain. As a result, the inversion produces a globally consistent estimate of the solution across the entire region, as shown in Fig. 5(b). As a remark, most large-scale SOLA-based seismic tomography studies have opted for choosing a (mostly) constant value for the trade-off parameter, while making the size of target kernels vary as a function of the local quality of data coverage (e.g. Zaroli 2016; Latallerie *et al.* 2022; Amiri *et al.* 2023; Freissler *et al.* 2024), with the advantage of lowering the total computational cost, as mentioned earlier. We emphasize again that this choice will be up to the practitioner and may depend on the size of the problem at hand.

To further validate the solution, we also examined the error estimates ($\sigma_{\hat{m}_k}$), which are shown in Fig. 6(a) together with the corresponding target kernel sizes (i.e. the radius ℓ_k) in Fig. 6(b). These error estimates demonstrate consistency across the inversion domain. In general, this numerical experiment highlights the effectiveness

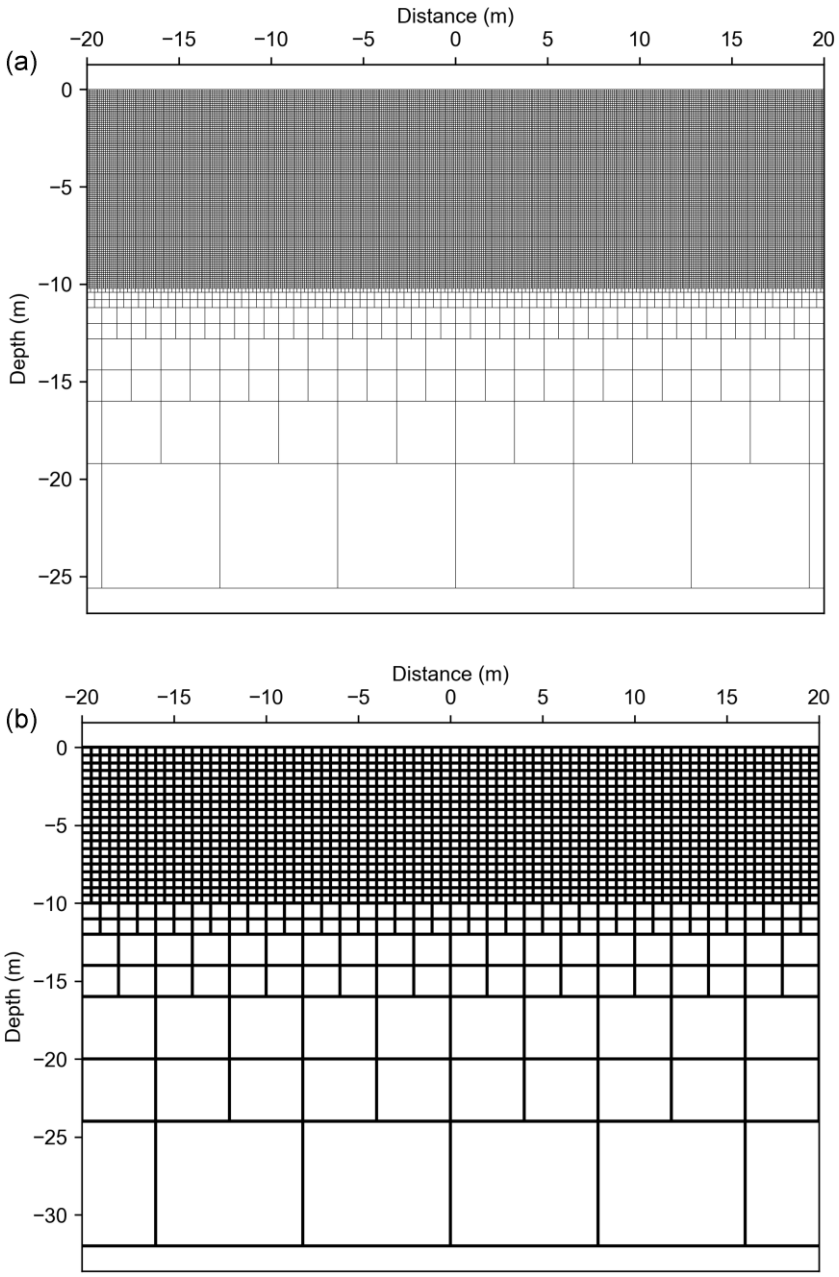

Figure 2. 'Toy' experiment: Quad-tree grids used for (a) modelling (i.e. the model grid) and for (b) the SOLA point-wise inversion (i.e. the set of all the inquiry points, which correspond to the centres of all the square cells).

of the SOLA algorithm in addressing the inversion problem in a computationally efficient manner while maintaining accuracy and consistency in the results.

6 SOLA INVERSION OF FIELD IP DATA

In this section, our aim is to apply the SOLA method for the inversion of a field IP data set, in a mineral exploration scenario. The Century zinc-lead-silver deposit in Australia has been the subject of many geophysical investigations (e.g. Oldenburg & Li 1999; Mutton 2000). We used the data shown in Fig. 7, which corresponds to the line 46800E of the DC resistivity and IP data set available in the SimPEG tutorial from Heagy (2020), corresponding to the measured apparent chargeability values and their associated standard deviations. We computed the SOLA estimates at all the inquiry locations $\mathbf{r}_k$ within the domain Ω. We chose each target kernel $T^{(k)}$ to be a circular disc centred on $\mathbf{r}_k$, since this means isotropic *a priori* resolution. The radius ℓ_k of $T^{(k)}$ represents the *a priori* resolving length around $\mathbf{r}_k$. As in earlier 2-D seismic tomography studies (e.g. Zaroli *et al.* 2017; Latallerie *et al.* 2022; Amiri *et al.* 2023), the radius ℓ_k was imposed to be correlated with the spatial data coverage, that is, a first-order proxy for *a priori* resolution. The size of the resulting target kernels $T^{(k)}$ is shown in Fig. 8(c). We also show, for reference the result of the inversion obtained using SimPEG (8d). We used the same strategy described in Section 5.3 for the selection of the resolution–uncertainty trade-off parameter η. Thus, we obtained the local average chargeabilities $\hat{m}_k$, see Fig. 8(a), with

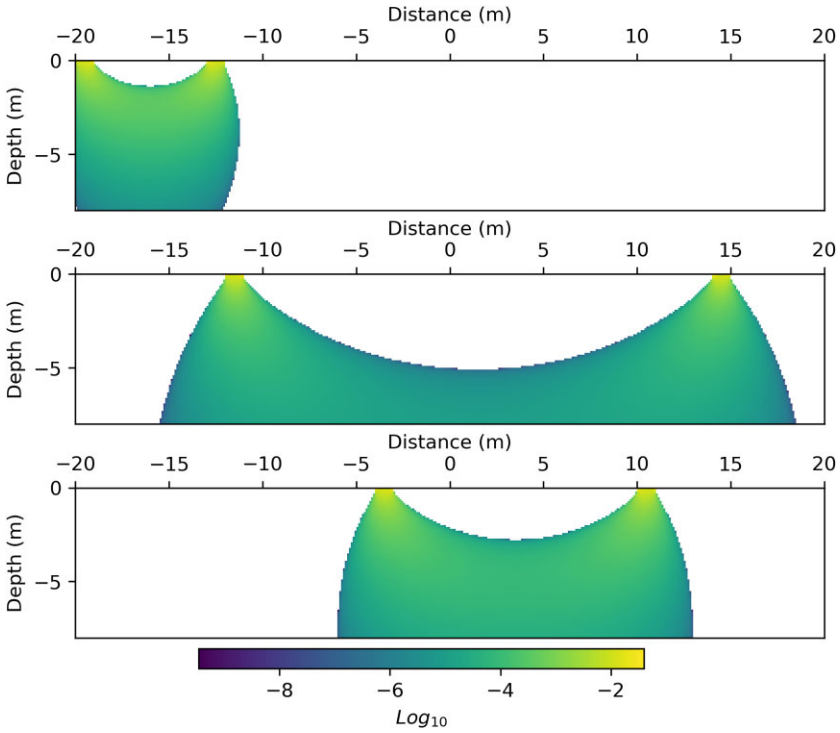

Figure 3. 'Toy' experiment: Three examples, for different dipole–dipole inter distances, of the ith row of the sensitivity matrix $\mathbf{G}$, which represents the ith data kernel $G_i(\mathbf{r})$ projected onto the model grid (used for modelling).

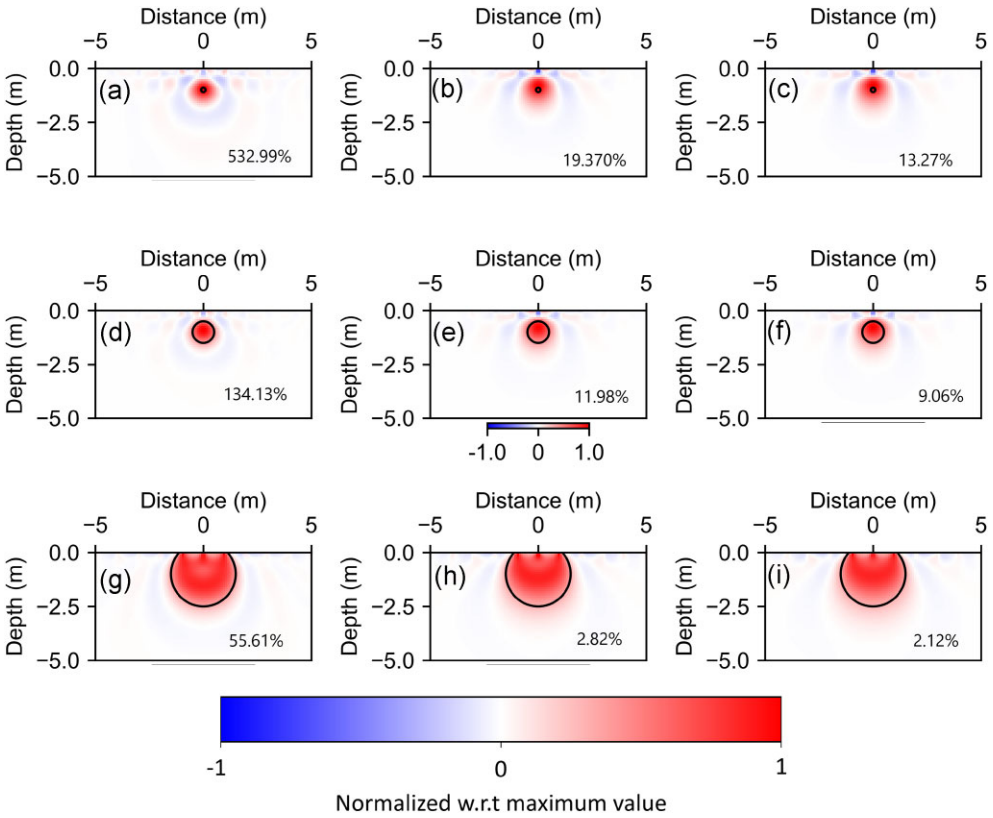

Figure 4. 'Toy' experiment: Gallery of SOLA averaging kernels obtained (from top to bottom) when increasing the size of the circular target kernel $T^{(k)}$, and (from left to right) when increasing the value of the trade-off parameter η. The percentages represent the model uncertainties $\sigma_{\hat{m}_k}$.

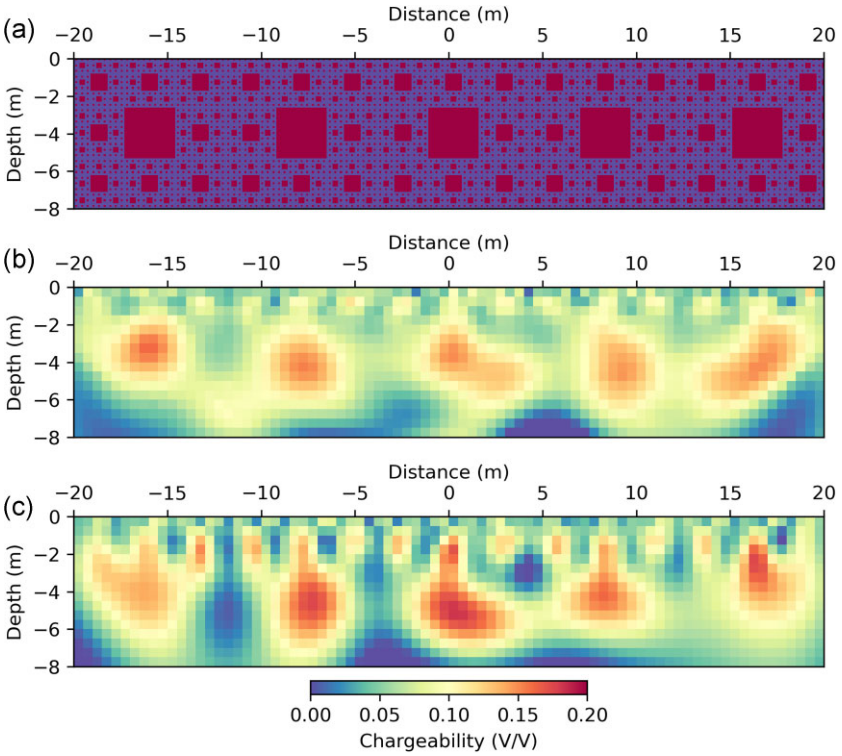

Figure 5. 'Toy' experiment: SOLA estimated local-average chargeabilities ($\hat{m}_k$). (a) True model, (b) SOLA solution and (c) SimPEG solution.

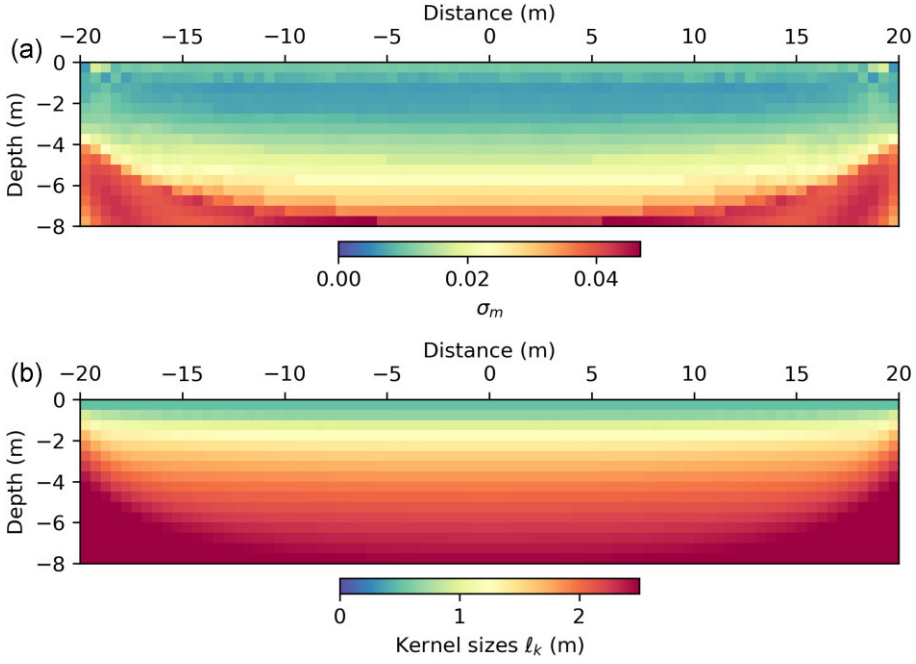

Figure 6. 'Toy' experiment: (a) SOLA estimated standard deviations, $\sigma_{\hat{m}_k}$; (b) target kernel radius, ℓ_k.

their uncertainties $\sigma_{\hat{m}_k}$, see Fig. 8(b), and their associated averaging kernels $A^{(k)}$. Examples of averaging kernels are shown in Fig. 9, at three particular inquiry points, labelled A, B and C, which will be used to highlight some specific properties of the SOLA results. Although SOLA is a *point-wise* reconstruction technique, we managed to recover a 'collection' of local-average estimates which altogether is *globally* geologically meaningful.

It is important to stress that a correct interpretation of the estimated averages needs to take into account the associated uncertainties and corresponding averaging kernels.

The bigger the averaging kernel support, the poorer the (local) resolution. The ideal case, of course, would be to have low uncertainties and small averaging kernel sizes, but, due to limitations of the physics and data acquisition layouts, such an optimal

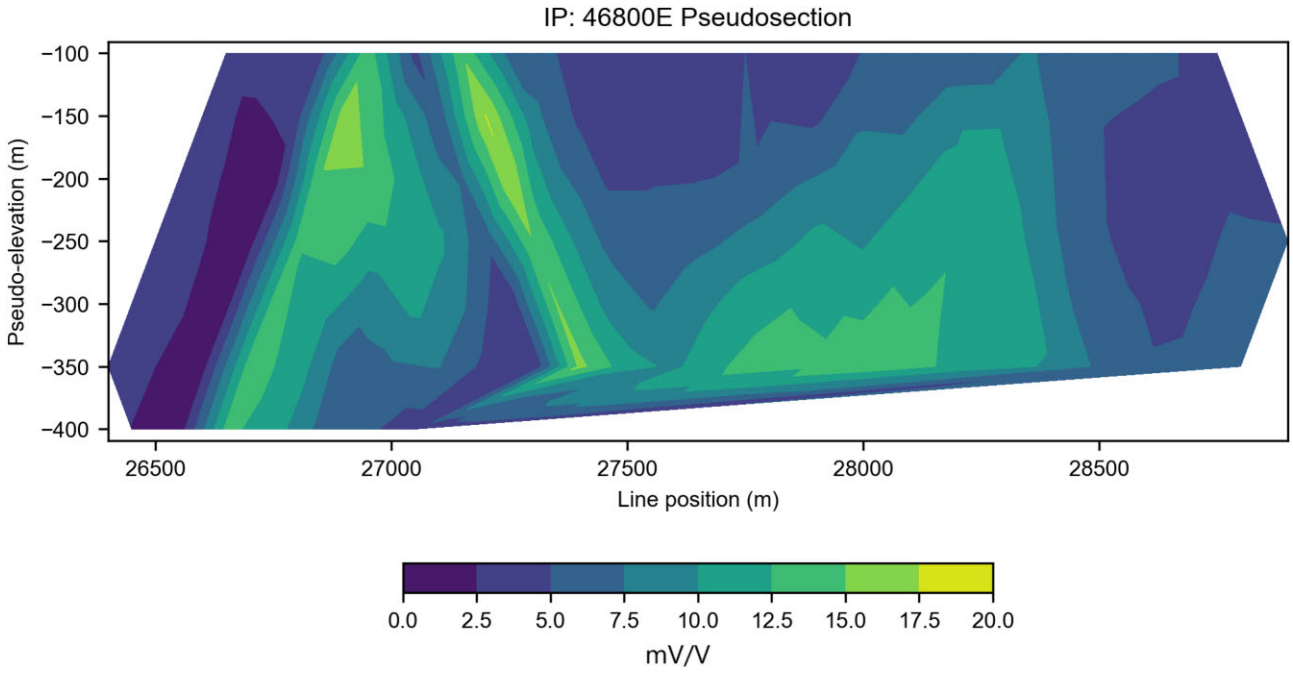

Figure 7. Century IP data for the line 46800E.

situation will seldom be achieved for the entire region in this particular scenario.

The size and shape of averaging kernels provide us with valuable information about *which properties* (local-average chargeabilities) of the unknown 'true' Earth can or cannot be inferred with confidence, given their uncertainties. The overall size of an averaging kernel reflects the local resolution and provides insight into the actual subregion that contributes to the local average. Fig. 9 shows that the actual resolving length at point B is shorter than at points A and C. Moreover, for points A and C, the averaging kernels are slightly displaced upward with respect to their inquiry points (green dots). We also note that their shapes are visibly different from the specified target kernels and that they contain negative side lobes near the surface. For point B, the averaging kernel is approximately well centred on its inquiry point and close to its target.

In summary, when the averaging kernel's shape (circular in this case) and its centre of mass deviate from the specified target kernel's shape and inquiry point, respectively, as for the points A and C, then the SOLA estimates are not well constrained and the interpretation/inference needs to be performed with more caution. These deficiencies were expected at points A and C, as they occur in places of poor data coverage and/or low sensitivity. Note that, in these situations, SOLA still gives us valuable information that can be used to further improve our data acquisition setup, to infer more robust properties at these locations.

Our SOLA-based analysis of the Century field data set forms a complete treatment of the DC/IP problem of inversion (inference). Besides computing estimates (local averages) for the chargeabilities, usually the only quantity estimated in classic inversions, we also obtained measures of the general uncertainty, that is, by analysing the estimated standard deviations and sizes of averaging kernels. Our chargeability estimates are in agreement with previous works (considering the fact that we are explicitly estimating averages), and our maps of uncertainties and averaging kernels are globally consistent. In general, the uncertainties are small, and the averaging-kernel sizes tend to increase in regions where the data coverage is poorer and/or the data sensitivity is reduced, that is, on the sides of the domain Ω and at increasing depth, as expected.

SOLA also offers a way towards painting a better portrait of the influence and limitations of the data acquisition setup and physics for this particular geophysical method, as applied to the estimation (inference) of rock chargeabilities. As a final remark, to take full advantage of SOLA, robust estimates of *data uncertainties* are required. Indeed, they are directly propagated into local-average uncertainties; see eq. (6). Since this task is often non-trivial across the communities, including the seismology and geophysical electromagnetic ones, this study also should motivate researchers to advance further the way DC/IP data uncertainties are estimated.

7 DISCUSSION

The SOLA tomographic scheme (Zaroli 2016) offers several advantages that complement standard inversion methods commonly used in the geophysical-electromagnetic community: (i) Localized and target-oriented solutions: SOLA provides a complete, localized solution to the (linear) IP inverse problem, solving independently for each enquiry point in the domain. (ii) Comprehensive uncertainty quantification: It simultaneously delivers the estimated local averages with their associated standard deviations and averaging kernels, the latter representing a measure of the local resolution. (iii) Unbiased averaging kernels: By design, the averaging kernels produced by SOLA are unbiased, unlike, for instance, the resolving kernels derived from damped least-squares inversions.

The SOLA approach is more efficient with regard to inversion approaches for the task of building a model (or model proxy) accompanied with information on its resolvability. However, traditional inversion techniques are more computationally efficient than SOLA if one wants to quickly build a model without such information. Indeed, if SOLA is applied to the entire inversion domain, it must be repeated, say, thousands of times, because it operates independently at each spatial point. Another way to think of SOLA

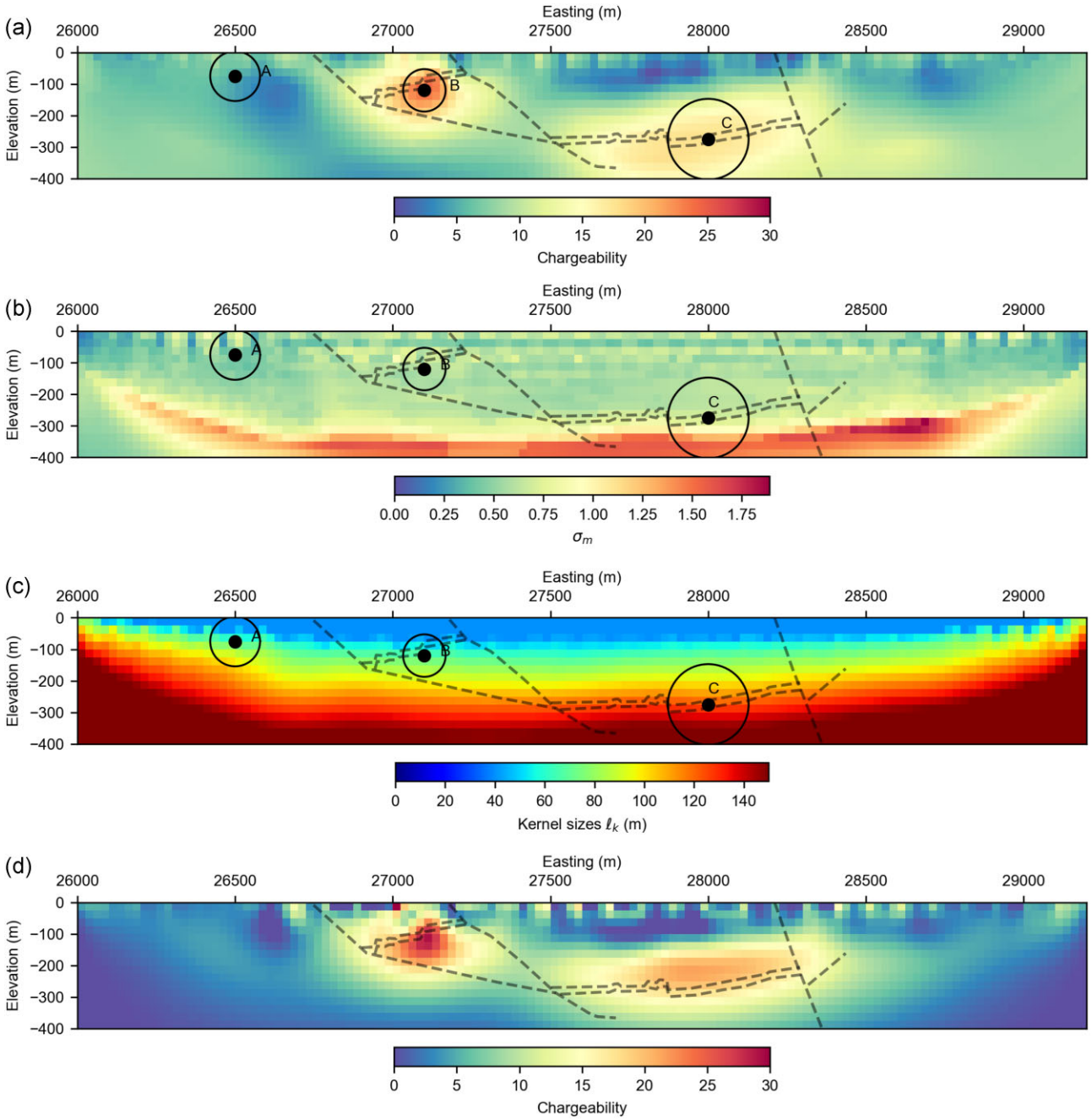

Figure 8. Century IP inversion: (a) SOLA estimated local-average chargeabilities ($\hat{m}_k$), with (b) their associated uncertainties (standard deviations $\sigma_{\hat{m}_k}$), and the (c) SOLA target kernel sizes (radius ℓ_k). In (d) we also show, for reference, the solution obtained using SimPEG.

is as an addition to other inversion techniques, not a replacement for them, depending on the situation. Performing a SOLA analysis for a few regions of particular interest, after analysing an initial model solution obtained for the entire domain using standard inversion approaches, would be a helpful workflow in this regard. Additionally, choosing appropriate target kernels and the trade-off parameter requires special attention. Although we have proposed a systematic strategy for their selection, it is still a topic that needs to be further investigated, including in the context of IP tomography.

Finally, despite the relatively higher computational demands, our numerical tests demonstrated that the SOLA method remains practical: for example, processing the synthetic test data took approximately 16 min on a laptop with 32GB of RAM, Intel 7 processor 3.8 GHz. It took much longer compared to under 10 s for a single inversion using SimPEG. Given that SOLA also offers information on the model's resolvability, whereas SimPEG does not for this comparison, this additional time is undoubtedly within acceptable bounds.

8 CONCLUSION

We have assessed, for the first time, the applicability of the SOLA tomographic method (Zaroli 2016) for the inversion of IP data. SOLA has allowed us to carry out quantitative resolution and uncertainty analysis of the obtained collection of local average chargeability

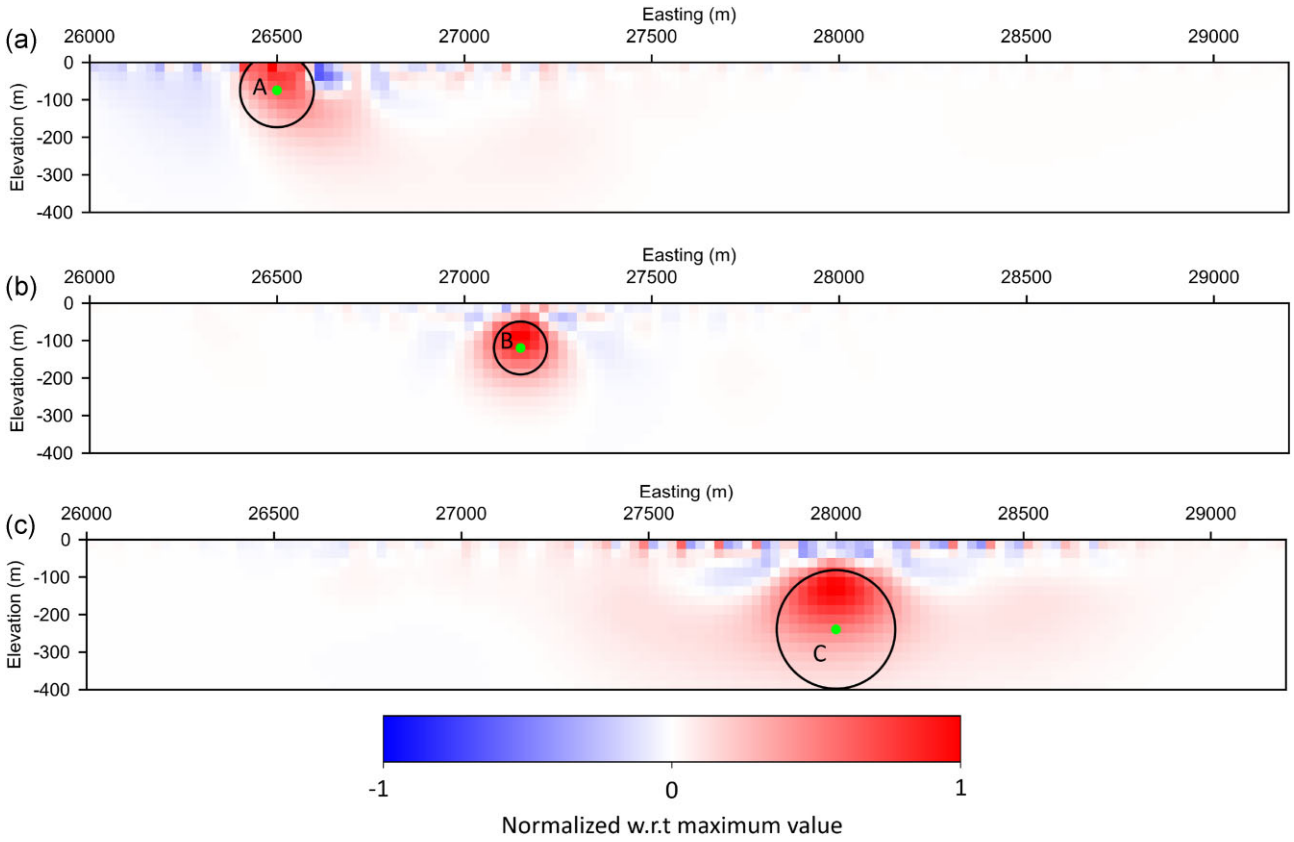

Figure 9. Century IP experiment: SOLA averaging kernels for three particular enquiry points. The black circles indicate the associated target kernels.

estimates. We have demonstrated the great potential and benefits of SOLA for applications with electric/electromagnetic geophysical data. It is still a computationally intensive technique; on the other hand, its point-wise estimation nature allows its use in a target-oriented manner. The analysis carried out in this study has the potential to be applied in a wide range of inversion scenarios in electrical and electromagnetic geophysics. We anticipate exciting future applications for this sophisticated and robust new inversion (inference) methodology.

ACKNOWLEDGMENTS

We thank the Editor (Line Meldgaard Madsen), Malcolm Sambridge and an anonymous reviewer for their constructive comments, which have substantially improved the manuscript. For this study we made use of GNU/Linux and Python (including packages Scipy, Numpy, Matplotlib).

DATA AVAILABILITY

The SimPEG code (Cockett *et al.* 2015) is used to compute the solution of DC resistivity, to set up the IP forward problem and IP sensitivity matrix, and is available at: https://simpeg.xyz/. The DC resistivity and IP data set (Heagy 2020) is used and available at: https://github.com/simpeg/transform-2020-simpeg. The 'discrete' version of SOLA tomography consists in running the LSQR algorithm (Paige & Saunders 1982) with specific, *study-dependent*, input matrices and vectors, corresponding to personal choices (e.g. data kernels, model discretization, target kernels), as detailed in Zaroli (2016)'s Appendix A. The LSQR code is available at (Stanford's Systems Optimization Laboratory): https://web.stanford.edu/group/SOL/software/lsqr/.

The Jupyter notebooks containing the code and data used for the tests can also be found at https://github.com/ghwilliams/GJI2025_SOLA_IP.

REFERENCES

Ahmed, A.S., Revil, A., Abdulsamad, F., Steck, B., Vergniault, C. & Guihard, V., 2020. Induced polarization as a tool to non-intrusively characterize embankment hydraulic properties, *Eng. Geol.,* **271,** doi: 10.1016/j.enggeo.2020.105604.

Amiri, S., Maggi, A., Tatar, M., Zigone, D. & Zaroli, C., 2023. Rayleigh wave group velocities in North-West Iran: SOLA Backus-Gilbert vs. Fast Marching tomographic methods, *Seismica,* **2**(2).

Angoran, Y. & Madden, T.R., 1977. Induced polarization: a preliminary study of its chemical basis, *Geophysics,* **42**(4), 788–803.

Aster, R.C., Borchers, B. & Thurber, C.H., 2018. *Parameter Estimation and Inverse Problems,* Elsevier.

Backus, G. & Gilbert, J.F., 1967. Numerical applications of a formalism for geophysical inverse problems, *Geophys. J. R. Astron. Soc,* **13,** 247–276.

Backus, G. & Gilbert, J.F., 1968. The resolving power of gross earth data, *Geophys. J. R. Astron. Soc.,* **16,** 169–205.

Backus, G. & Gilbert, J.F., 1970. Uniqueness in the inversion of inaccurate gross earth data, *Phil. Trans. R. Soc. A,* **266**(1173), doi: 10.1098/rsta.1970.0005.

Bleil, D.F., 1953. Induced polarization: a method of geophysical prospecting, *Geophysics,* **18,** 636–661.

Cockett, R., Kang, S., Heagy, L.H., Pidlisecky, A. & Oldenburg, D.W., 2015. SimPEG: An open source framework for simulation and gradient based

parameter estimation in geophysical applications, *Comput. Geosci.,* **85,** 142–154.

Freissler, R., Schuberth, B. S. A. & Zaroli, C., 2024. A concept for the global assessment of tomographic resolution and uncertainty, *Geophys. J. Int.,* **238**(2), 992–1012.

Gurin, G., Titov, K., Ilyin1, Y. & Tarasov, A., 2015. Induced polarization of disseminated electronically conductive minerals: a semi-empirical model, *Geophys. J. Int.,* (200), 1555–1565.

Haario, H. & Somersalo, E., 1987. The backus-gilbert method revisited: background, implementation and examples, *Num. Funct. Anal. Optimiz.,* **9**(9&10), 917–943.

Hallof, P.G., 1957. On the interpretation of resistivity and induced polarization field measurements, *MIT Thesis*.

Heagy, L., 2020. Transform 2020 - geophysical inversions with simpeg, accessed 13 march 2024.Transform 2020 - Geophysical inversion with SimPEG

Jackson, D.D., 1972. Interpretation of inaccurate, insufficient, and inconsistent data, *Geophys. J. Int.,* **28**(2), 97–109.

Kirsch, A., Schomburgi, B. & Berend, G., 1988. The Backus-Gilbert method, *Inverse Probl.,* **4,** 771–783.

Latallerie, F., Zaroli, C., Lambotte, S. & Maggi, A., 2022. Analysis of tomographic models using resolution and uncertainties: a surface wave example from the Pacific, *Geophys. J. Int.,* **230**(2), 893–907.

Leitão, A., 1998. Applications of the Backus-Gilbert method to linear and some nonlinear equations, *Inverse Probl.,* **14,** 1285–1297.

Li, Y. & Oldenburg, D.W., 2000. 3-D inversion of induced polarization data, *Geophysics,* **65**(6), 1931–1945.

Mag, A., Zaroli, C. & Koelemeijer, P., 2025. Bridging the gap between SOLA and deterministic Linear Inferences in the context of seismic tomography, *Geophys. J. Int.,* **242,** doi: 10.1093/gji/ggaf131.

Marshall, D.J. & Madden, T.R., 1959. Induced polarization, a study of its causes, *Geophysics,* **24**(4), 790–816.

Mutton, A.J., 2000. The application of geophysics during the evaluation of the century zinc deposit, *Geophysics,* **65,** 1946–1960.

Nolet, G., 2008. *A Breviary of Seismic Tomography,* Cambridge Univ. Press.

Oldenburg, D.W. & Li, Y., 1994. Inversion of induced polarization data, *Geophysics,* **59,** 1327–1341.

Oldenburg, D.W. & Li, Y., 1999. Estimating depth of investigation in DC resistivity and IP surveys, *Geophysics,* **64,** 403–416.

Paige, C.C. & Saunders, M., 1982. Lsqr: An algorithm for sparse, linear equations and sparse least squares, *A.C.M. Trans. Math. Softw.,* **8,** 43–71.

Pijpers, F.P., 1997. Chavent, Get al. (eds.), *Inversions in astronomy and the SOLA method, in Inverse Problems in Wave Propagation* Springer Science + Business Media, pp. 419–442.

Pijpers, F.P. & Thompson, M.J., 1992. Faster formulations of the optimally localized averages method for helioseismic inversions, *Astron. Astrophys.,* **262,** L33–L36.

Pijpers, F.P. & Thompson, M.J., 1994. The SOLA method for helioseismic inversion, *Astron. Astrophys.,* **281,** 231–240.

Pujol, J.M., 2013. The Backus-Gilbert method and their minimum-norm solution, *Geophysics,* **78**(3), W9–W30.

Revil, A., Ghorbani, A., Su, Z., Cai, H. & Hu, X., 2024. Induced polarization of clay-rich materials. 3. partially saturated mixtures of clay and pyrite, *Geophysics,* **89**(3), E101–E112.

Rijo, L., 1984. Inversion of three-dimensional resistivity and induced polarization data, *SEG Technical Program Expanded Abstracts,* 113–117.

Seigel, H.O., 1959. Mathematical formulation and type curves for induced polarization, *Geophysics,* **24,** 547–565.

Snieder, R., 1991. An extension of Backus-Gilbert theory to nonlinear inverse problems, *Inverse Probl.,* **7,** 409–433.

Sumner, J.S., 1976. *Principles of Induced Polarization for Geophysical Exploration,* Elsevier.

Tarantola, A., 2006. Popper, Bayes and the inverse problem, *Nature Phys.,* **2**(8), 492–494.

Tikhonov, A.N. & Arsenin, V.A., 1977. *Solutions of ill-Posed Problems,* V. H. Winston & Sons.

Vacquier, V., Holmes, C.R., Kintzer, P.R. & Lavergne, M., 1957. Prospecting for groundwater by induced electrical polarization, *Geophysics,* **22**(3), 660–697.

Zaroli, C., 2016. Global seismic tomography using Backus-Gilbert inversion, *Geophys. J. Int.,* **207,** 876–888.

Zaroli, C., 2019. Seismic tomography using parameter-free Backus-Gilbert inversion, *Geophys. J. Int.,* **218**(1), 619–630.

Zaroli, C., 2021. *Seismic Tomography using SOLA-Backus-Gilbert inversion,* Ph.D. thesis, Habilitation (HDR), University of Strasbourg.

Zaroli, C., Koelemeijer, P. & Lambotte, S., 2017. Toward seeing the earth's interior through unbiased tomographic lenses, *Geophys. Res. Lett.,* **44,** 11399–11408.